

# Dispersion engineering and measurement in crystalline microresonators using a fiber ring etalon

XIAOBAO ZHANG,<sup>1,2</sup> GUOPING LIN,<sup>1,\*</sup> TANG SUN,<sup>1</sup> QINGHAI SONG,<sup>1</sup> GUANGZONG XIAO,<sup>2,3</sup> AND HUI LUO<sup>2</sup>

<sup>1</sup>Ministry of Industry and Information Technology Key Laboratory of Micro-Nano Optoelectronic Information System, School of Science, Harbin Institute of Technology, Shenzhen 518055, China

<sup>2</sup>College of Advanced Interdisciplinary Studies, National University of Defense Technology, Changsha 410073, China

<sup>3</sup>e-mail: xiaoguangzong@nudt.edu.cn

\*Corresponding author: guoping.lin@hit.edu.cn

Received 2 July 2021; revised 27 August 2021; accepted 30 August 2021; posted 1 September 2021 (Doc. ID 435837); published 21 October 2021

Dispersion engineering and measurement are significant for nonlinear photonic applications using whispering gallery mode microresonators. Specifically, the Kerr microresonator frequency comb as an important example has attracted a great amount of interest in research fields due to the potential capability of full integration on a chip. A simple and cost-efficient way for dispersion measurements is thereby in high demand for designing such a micro-comb device. Here, we report a dispersion measurement approach using a fiber ring etalon reference. The free spectral range of the etalon is first measured through sideband modulation, and the dispersion of the etalon is inferred by binary function fitting during the dispersion measurement. This method is demonstrated on two MgF<sub>2</sub> disk resonators. Experimental results show good agreement with numerical simulations using the finite element method. Dispersion engineering on such resonators is also numerically investigated. © 2021 Chinese Laser Press

<https://doi.org/10.1364/PRJ.435837>

## 1. INTRODUCTION

Optical microresonators with small mode volumes and ultra-high quality ( $Q$ ) factors can significantly decrease the threshold power of parametric oscillations, which makes them an ideal platform for optical frequency comb generation [1–6]. Since Kerr frequency combs were demonstrated in a silica toroidal cavity in 2007 [7], they have been utilized in applications such as spectroscopy [8,9], optical atomic clocks [10,11], astronomical calibration [12,13], coherent communications [14,15], low-noise frequency synthesis [16,17], laser ranging [18–20], and photonic convolutional processing [21,22]. Dispersion as one of key parameters of Kerr microcombs, usually referred to as the group velocity dispersion (GVD) of cavity modes, is preferred to be in the anomalous regime [2,23–27]. Although Kerr frequency combs can be obtained in the normal dispersion regime under some special conditions [28–33], the spectral width is typically limited. Moreover, the dispersive wave caused by the optical analog of Cherenkov radiation may occur when a Kerr soliton comb extends into a region where second order dispersion changes sign [34]. These waves play an important role in spectral control and can provide quiet states of soliton comb operation [35]. In addition, the dispersion of microresonators has a large influence on quantum optics, which needs high coherences [36,37].

The dispersion of microresonators is mainly determined by two parts: material and geometric dispersion. Therefore, dispersion engineering is realized by controlling these two parts. Extensive works have been contributed in this field. For instance, HfO<sub>2</sub>-coated Si<sub>3</sub>N<sub>4</sub>, oxidized Si resonators, and hybrid waveguides of AlGaIn and AlN have been studied to apply multiple host materials for material dispersion engineering [38–40]. Geometry dispersion can be realized through changing the dimension of the waveguide cross section such as rectangular waveguides with different widths and heights, concentric structures of Si<sub>3</sub>N<sub>4</sub>, wedge and double-wedge shapes of SiO<sub>2</sub>, and microstructured boundaries of crystalline disk resonators [41–45]. Hence, microresonator dispersion measurement is highly demanded in this field.

There have been several methods for the measurement of the microresonator dispersion [46]. One of the common ways is frequency-comb-based spectroscopy [47–49]. In this way, the frequency-comb laser intervenes with the scanning continuous-wave laser, which is injected in the microresonator. Then the beat signals of the two lasers are like a ruler and provide information of the scanning laser frequency. Another method is sideband spectroscopy based on electro-optic modulation [43,50,51]. Usually, an electro-optic phase modulator is utilized to generate sidebands of the scanning laser. The frequency

difference between the sidebands and pump is equivalent to the modulation frequency generated by a radio-frequency (RF) source. Therefore, the laser frequency is linked with the known RF signals, and dispersion can be obtained. Although these two methods can provide high-precision dispersion measurements, the requirement of a commercial frequency comb laser or a tunable microwave source that can reach about one free spectral range (FSR) of the microresonator is usually difficult to meet for regular laboratory conditions. Thereby, other methods have been developed. For instance, a price-friendly fiber Mach-Zehnder interferometer (MZI) can be applied in dispersion measurement [52–54]. However, it usually needs to be calibrated by the two methods mentioned before, as it is difficult to get its FSR and dispersion from MZI fringes [46].

In this paper, we introduce a dispersion measurement method based on a fiber ring cavity that is cheap and easy to access. The FSR of the fiber cavity can be easily designed to be few tens of MHz. Moreover, unlike MZI, its FSR can be directly calibrated with a regular in-laboratory function generator without the presence of microresonators. Assisted by binary function fitting of the measurement data, the dispersion of the fiber cavity is assessed. Finally, the data can be used to derive the dispersion profile of the whispering gallery mode (WGM) family. The method is demonstrated on two MgF<sub>2</sub> resonators with different cross sections. Experimental results meet our simulations obtained using the finite element method (FEM). Numerical investigation of dispersion engineering in such resonators is also carried out.

## 2. THEORY AND METHODS

The resonance frequency intervals between adjacent longitudinal modes should be the same in an ideal optical resonator without dispersion. Hence, the relative positions of the resonance frequencies can be used to characterize resonator dispersion. Generally, the resonance frequencies  $\omega_\mu$  of a mode family can be expressed in a form of Taylor expansion [26,52,55]:

$$\begin{aligned}\omega_\mu &= \omega_0 + D_1\mu + \frac{1}{2}D_2\mu^2 + \sum_{j>2} \frac{1}{j!}D_j\mu^j \\ &= \omega_0 + D_1\mu + D_{\text{int}},\end{aligned}\quad (1)$$

where  $\mu$  is the relative mode number, and  $\mu = 0$  corresponds to the central mode, which is around 1550 nm.  $D_1$ ,  $D_2$  characterize the equidistant resonator FSR and second order dispersion, respectively.  $D_{\text{int}}$  is the sum of the nonlinear terms, which represents the influence of dispersion, and  $\omega_0$  is the resonance frequency of the central mode. In most cases, only second order dispersion is considered as  $D_1 \gg D_2 \gg D_j$  ( $j > 2$ ).

The schematic of this dispersion measurement method is shown in Fig. 1(a). In the experiment, an external cavity diode laser (ECDL) with a linewidth of 10 kHz is used as the light source, and the transmission spectra of the two cavities are recorded at the same time with a four-channel oscilloscope. The fiber ring etalon is prepared using a  $2 \times 2$  90:10 fiber coupler with two ports connecting (10% output port connected with another input port) through a single mode fiber. The FSR of the etalon thereby is determined by the fiber loop length. For

clarity, a fiber polarizer is added to ensure single polarized mode operation within one FSR when scanning the laser as shown in Fig. 1(b). Also, the resonance frequency of resonators is affected by temperature. The thermo-optical coefficient of silica is about  $1.19 \times 10^{-5} \text{ K}^{-1}$ , which means the resonance frequency drift caused by temperature changing is about 2 MHz/mK at 1550 nm [56]. This thermal frequency drift reduces the accuracy of measurement, and sometimes the relative frequency shift between the fiber cavity resonance and MgF<sub>2</sub> microresonator resonance can exceed 160 MHz/min. Considering that the maximum value of  $D_{\text{int}}$  we measured in the experiment is about dozens of MHz, this temperature drift cannot be ignored. Thus, a silicone rubber heater is utilized to keep the temperature of the fiber cavity stable through proportional-integral-derivative (PID) control. The thermo-optical coefficient of MgF<sub>2</sub> is more than an order of magnitude smaller than that of silica [57]. Hence, it is found that even if the temperature control is applied only on the fiber cavity, the relative frequency shift can be already smaller than 5 MHz/min.

As the transmission spectra of the fiber cavity and the MgF<sub>2</sub> microresonator are obtained simultaneously, every resonance frequency of the microresonator can be expressed in the form of the corresponding resonance frequency of the fiber cavity. However, the resonance frequency of the fiber cavity usually is not coincident with that of the microresonator. Here a rational parameter  $\mu_F$  is defined as the corresponding mode number of microresonator mode  $\mu$ , and its absolute value is equal to the number ( $n$ ) of complete periods of fiber cavity FSR plus the residual non-integer periodic number ( $t_\mu/T_\mu$ ) between mode  $\mu$  and the central mode of the fiber cavity [see Fig. 1(e)]. Hence, the resonance frequency of mode  $\mu$  can be expressed in a form of  $\mu_F$ :

$$\omega_\mu = \omega_{0_F} + D_{1F}\mu_F + D_{\text{int}F} \approx \omega_{0_F} + D_{1F}\mu_F + \frac{1}{2}D_{2F}\mu_F^2, \quad (2)$$

where  $\omega_{0_F}$ ,  $D_{1F}$ ,  $D_{2F}$ ,  $D_{\text{int}F}$  represent the central mode resonance frequency, equidistant FSR, second order dispersion, and total dispersion of the fiber cavity, respectively. Equation (2) appears similar to Eq. (1); however, it should be noted that  $\mu$  is an integer, and  $\mu_F$  is a rational number corresponding to  $\mu$  in a form of fiber cavity mode periods. Then the frequency difference between mode  $\mu$  and the central mode can be expressed as

$$\Delta\omega_\mu = \omega_\mu - \omega_0 \approx D_1\mu + \frac{1}{2}D_2\mu^2 = D_{1F}\mu_F + \frac{1}{2}D_{2F}\mu_F^2 + \Delta\omega_0, \quad (3)$$

where  $\Delta\omega_0$  is defined as the frequency difference between  $\omega_0$  and  $\omega_{0_F}$ . Figure 1(e) shows how Eq. (3) is acquired and the definition of the parameters as an example of  $\mu = -1$ . Hence, the dispersion influence  $D_{\text{int}}$  appears as

$$D_{\text{int}} \approx \frac{1}{2}D_2\mu^2 = D_{1F}\mu_F - D_1\mu + \frac{1}{2}D_{2F}\mu_F^2 + \Delta\omega_0. \quad (4)$$

Particularly, a parameter  $D'_{\text{int}}$  that includes dispersion of the fiber cavity is defined as

$$D'_{\text{int}} = D_{\text{int}} - D_{\text{int}F} \approx D_{1F}\mu_F - D_1\mu + \Delta\omega_0. \quad (5)$$

From Eq. (5), it is found that  $D'_{\text{int}}$  is a binary function of  $\mu$  and  $\mu_F$ , and the fitting is based on this formula. The measurement

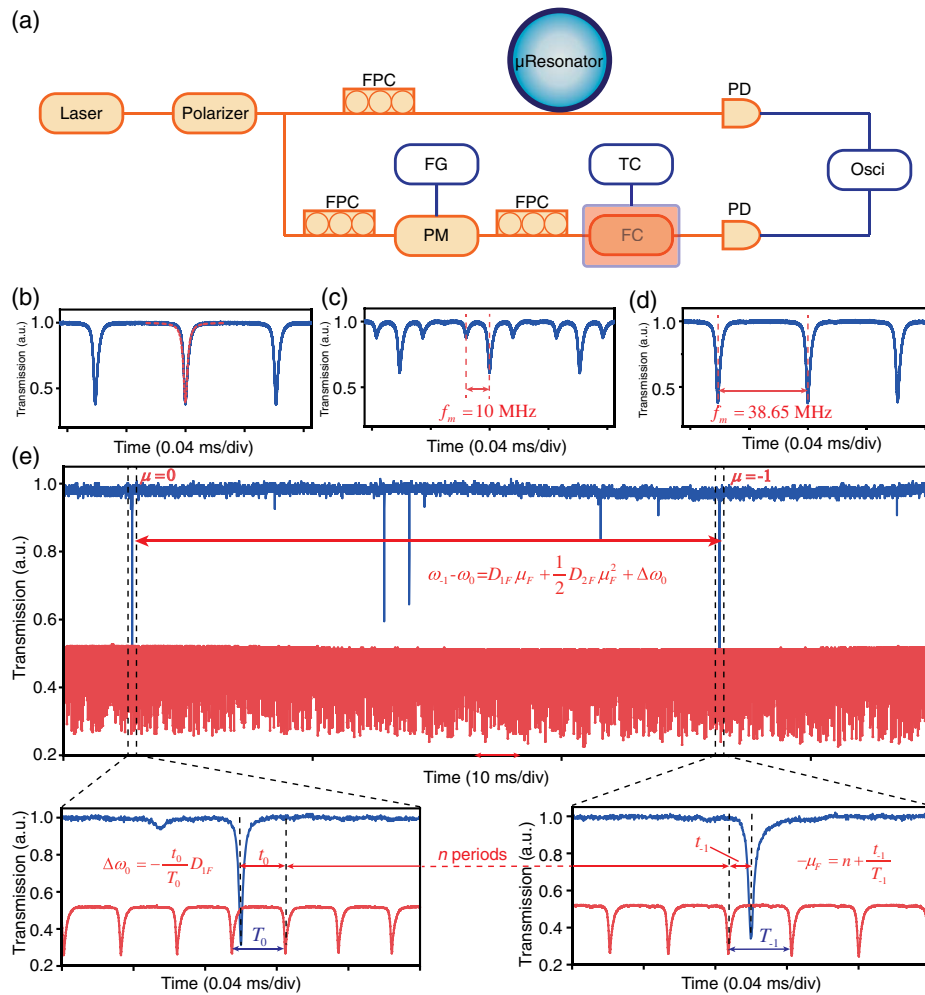


**Fig. 1.** (a) Schematic of the experiment setup. Orange lines denote optical paths, and blue lines represent electric cables. A tapered fiber is employed to couple the laser in and out of the microresonator. The fiber cavity is put on a silicone rubber heater, and both of them are kept in a thermal insulation box. Temperature is set as 50°C in the experiment. FPC, fiber polarization controller; FG, function generator; PM, phase modulator; TC, temperature controller; FC, fiber cavity; PD, photodiode. (b) Transmission spectrum of the fiber cavity without phase modulation. The red dashed line is Lorentz fitting for the resonance, and the fitting shows that the loaded  $Q$  of this fiber cavity mode is about 97 million. (c) Transmission spectrum of the fiber cavity when modulation frequency is 10 MHz. Two small dips in one FSR are caused by the resonance between sidebands and fiber cavity. (d) Transmission spectrum of the fiber cavity when modulation frequency is equal to one FSR of the cavity. In this situation, the transmission spectrum is almost the same as the one without phase modulation. (e) Measured microresonator transmission spectrum (blue) and etalon signal (red) of one microresonator FSR. The laser is scanned from short to long wavelength. Two small figures below the larger one are enlarged views.

process can be divided into three steps. First, FSR of the fiber cavity at 1550 nm is measured by the electro-optic sideband method. Specifically, as shown in Fig. 1(c), two sidebands generated by a phase modulator can also resonate with the fiber cavity, and this induces two more resonance dips on the transmission spectrum. As part of the pump power is used to generate sidebands, the transmission of pump resonance increases. When the modulation frequency ( $f_m$ ) nearly matches the fiber cavity FSR, the three dips can overlap each other and become one resonance dip [46]. Then  $f_m$  is finely tuned to make the dip deepest, and now the modulation frequency is equal to the cavity FSR, namely,  $D_{1F}/2\pi = f_m$ . As the FSR of the fiber cavity is about dozens of MHz, which is much smaller than that of WGM resonators (WGMs) (at least dozens of

GHz), a general function generator can be used as the RF source, and the cost reduces significantly compared to previous sideband spectrum methods. Second, the measurement data are processed according to Eq. (5), and the binary function fitting is conducted on the processed data. In this step,  $\mu$ ,  $\mu_F$ , and  $\Delta\omega_0$  can be directly obtained from measurement. Also,  $D_1$  is estimated as  $D_1 \approx (|\Delta\omega_1| + |\Delta\omega_{-1}|)/2$  without consideration of fiber cavity dispersion, and the estimated  $D_1$  can be finely adjusted to ensure that the scatter diagram of  $D_{\text{int}}^i$  and  $\mu$  is symmetric about  $\mu = 0$ . The detailed fitting process will be demonstrated in Section 4. Finally, after acquiring  $D_{2F}$ , the measurement data are reprocessed based on Eq. (4), and a quadratic fitting is utilized to get  $D_2$ , which characterizes the dispersion of the WGM.

### 3. NUMERICAL EVALUATIONS OF WGM DISPERSION

Previous studies reveal that FEM is a reliable way to calculate microresonator dispersion, and its results are in good agreement with experimental ones [43,46,51]. Hence, FEM has been widely used in microresonator dispersion engineering. The numerical results can assist binary function fitting and provide a good assessment of the etalon reference. It is vital to build an effective geometrical model for FEM calculation as the material of the resonators is determined. Although the analytical approximation of eigenfrequencies of WGMs in toroidal disks has been used to investigate cavity dispersion for Kerr combs [58], FEM can provide better accuracy and flexibility. As shown in Fig. 2(a), different from previous spheroid models of MgF<sub>2</sub> resonators [46], the cross section of the resonator boundary is characterized by an arc connected with two oblique lines. The geometry of one MgF<sub>2</sub> microresonator is described by five parameters, namely, the major radius  $R$ , arc radius  $r$ , length of the arc area  $h$ , and two angles between two oblique lines and horizontal line  $\theta_1, \theta_2$ . An optical microscope is used to measure the geometrical contours of two WGMs, called WGMR A and WGMR B.

Different transverse azimuthal modes of these two microresonators are investigated by FEM. The mode index  $p$  represents different orders in the azimuthal direction. Although disk resonators also feature different radial modes, they could show normal dispersion, which is not preferable for comb generation. Figures 3(a) and 3(b) give calculated field distributions of different azimuthal modes, and their corresponding  $D_{\text{int}}/2\pi$  are

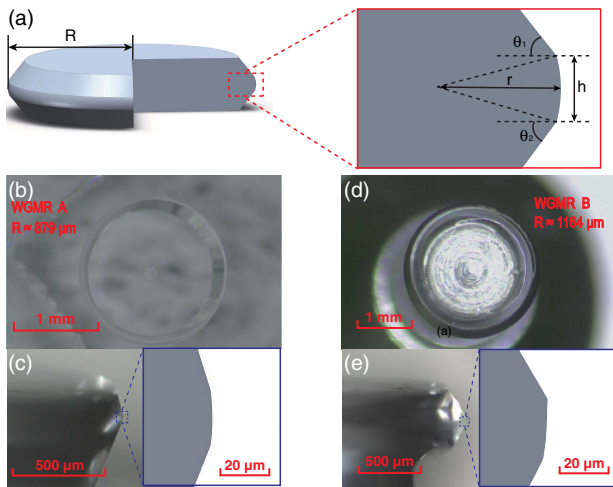


**Fig. 2.** (a) Geometric model of MgF<sub>2</sub> microresonators. The left panel is an enlarged view of the microresonator boundary where light transmits. (b) Top view of WGMR A mounted on a glass plate. The measured main radius  $R$  is about 879  $\mu\text{m}$ . (c) Front view of WGMR A. The right panel is the geometry used in FEM, which is obtained from the left panel by zooming in. In this model,  $r \approx 86 \mu\text{m}$ ,  $h \approx 23 \mu\text{m}$ ,  $\theta_1 \approx 73^\circ$ ,  $\theta_2 \approx 68^\circ$ . (d) Top view of WGMR B mounted on a post. The measured main radius  $R$  is about 1164  $\mu\text{m}$ . (e) Front view of WGMR B. The right panel is the geometry used in FEM, which is obtained from the left panel by zooming in. The arc area is rotated to make the model more coincident with the real one. In this model,  $r \approx 176 \mu\text{m}$ ,  $h \approx 24 \mu\text{m}$ ,  $\theta_1 \approx 60^\circ$ ,  $\theta_2 \approx 63^\circ$ .

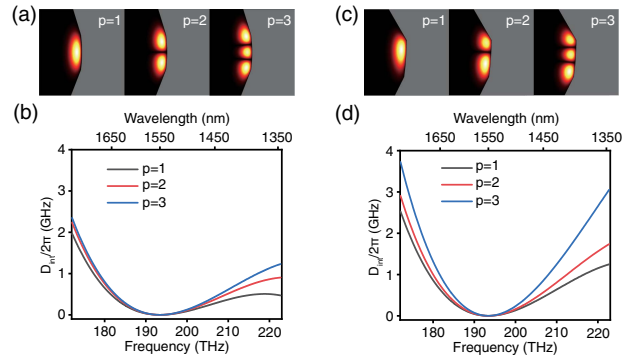


**Fig. 3.** (a) Electric field distribution of WGMR A with different azimuthal mode indices. (b) Simulation dispersion plot of  $D_{\text{int}}$  versus laser frequency of WGMR A. The resonator FSR acquired from the calculation is about 39.4 GHz. (c) Electric field distribution of WGMR B with different azimuthal mode indices. (d) Simulation dispersion plot of  $D_{\text{int}}$  versus laser frequency of WGMR B. The resonator FSR acquired from the calculation is about 29.5 GHz.

also shown in Figs. 3(c) and 3(d). It is obvious that higher order azimuthal modes have larger dispersion, and  $D_{\text{int}}$  within a small spectral window (1530–1570 nm) can be seen as being contributed only by second order dispersion.

The influence of geometry parameters on WGM dispersion is also studied by FEM. Figure 4 demonstrates the calculation results of different geometry parameter settings of various azimuthal modes. In each subplot, except the scanning parameter, the other parameters remain unchanged in the calculation. The general settings are  $r = 100 \mu\text{m}$ ,  $h = 25 \mu\text{m}$ ,  $\theta_1 = \theta_2 = 60^\circ$ . Also, as  $\theta_1$  and  $\theta_2$  are equivalent in geometry dispersion, Fig. 4(d) gives the results of scanning  $\theta$ , which is defined as  $\theta = \theta_1 = \theta_2$ . Namely, these two angles have the same value and change simultaneously in this subplot.

It is obvious from Fig. 4 that dispersion values of all three azimuthal modes have similar trend patterns with the specific

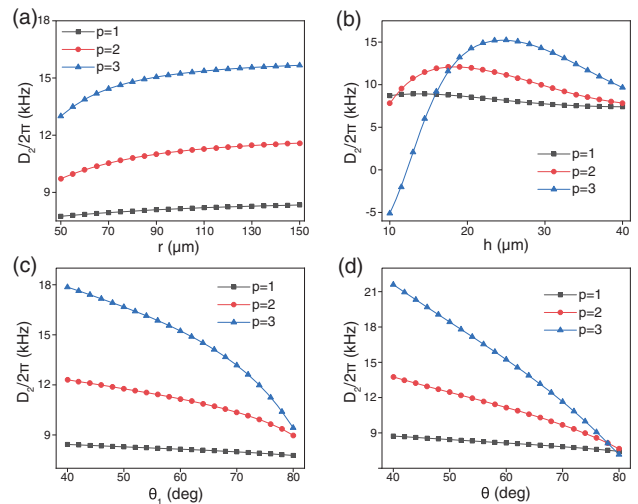


**Fig. 4.** Calculated  $D_2/2\pi$  with different (a)  $r$ , (b)  $h$ , (c)  $\theta_1$ , and (d)  $\theta$  of various azimuthal modes. In all calculations, the major radius of the microresonator is set as 879  $\mu\text{m}$ , which is coincident with that of WGMR A.

geometry parameter scanning. However, higher order azimuthal modes are more sensitive to geometry parameters, as they show larger fluctuations in dispersion values. This could be explained by the fact that higher order azimuthal modes feature larger mode areas and their mode distributions can be easily influenced by boundary geometry changes. Moreover, compared to other geometry parameters,  $r$  seems to have a smaller influence on dispersion, and a small  $b$  may induce a negative  $D_2$ , which is not preferable for frequency comb generation. Hence, in these parameter settings,  $\theta_1$ ,  $\theta_2$  may be more suitable for dispersion engineering.

#### 4. RESULTS AND DISCUSSION

In the measurement, the laser scanning speed is set as 10 nm/s, and scanning range is 1530–1570 nm. The sampling rate of the oscilloscope is 5 MSa/s. Since the laser scanning speed is not

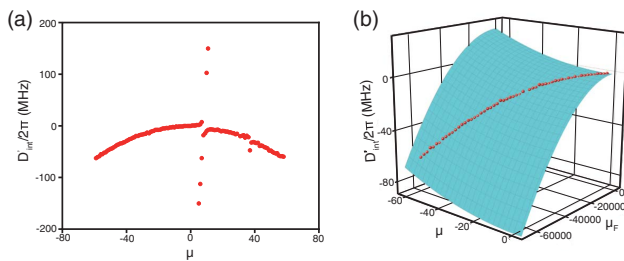


**Fig. 5.** (a) Measurement dispersion  $D'_{\text{int}}$  versus relative mode number  $\mu$ . The measurement data are acquired from WGMR A. There is an obvious avoided mode crossing near the central mode. The right part of the plot is affected by several small mode crossings, which obviously decreases its ideality. (b) Binary fitting of measurement dispersion  $D'_{\text{int}}$ . The parameters obtained from this fitting are  $D_2/2\pi = 10.3$  kHz,  $D_{2F}/2\pi = 43.5$  mHz,  $a/2\pi = 8.5$  kHz,  $b/2\pi = -343$  kHz. Adjusted  $R^2$  of the fitting is about 0.9991.

constant through the whole operation, we choose to analyze the central data. The actual number of sampling points is about 23 million per channel for one scan, which means that the sampling precision of the laser frequency is about 200 kHz. The measurement data of WGMR A are processed based on the method introduced in Section 2. Figure 5(a) demonstrates the dispersion parameter including fiber cavity dispersion  $D'_{\text{int}}$  with the relative mode number  $\mu$ . The equation used for binary function fitting differs from Eq. (5) considering some realities, and it appears as

$$D'_{\text{int}} = \frac{1}{2}D_2\mu^2 - \frac{1}{2}D_{2F}\mu_F^2 + a\mu + b, \quad (6)$$

where the significance of  $a$  lies in the calibration for  $D_1$ , as  $D_1$  is an estimated number. However, it should not have a calibration for  $D_{1F}$ , while the value of  $D_1$  is based on the value of  $D_{1F}$ , and a calibration for  $D_{1F}$  will compensate for the value change of  $D_1$ . Similarly,  $b$  is introduced as a result of the measuring error and the influence of an avoided mode crossing near the central mode [59]. As the right half ( $\mu > 0$ ) of  $D'_{\text{int}}$  is obviously affected by avoided mode crossings (spur-like features), only the left half is utilized for fitting. Some fitting parameters, for example, starting points and boundaries, are set based on the FEM results, and the fitting results are shown in Fig. 5(b).

As described in Section 2, the parameters obtained from binary function fitting are used to reprocess the measuring data according to Eq. (4). Then a quadratic fitting is applied in the reprocessed data to get  $D_2/2\pi$ . Mode index  $p$  of the WGM is inferred by the FEM combined with the measurement dispersion results. The transmission of the WGM used for calibration is shown in Fig. 6(a), and Fig. 6(b) demonstrates the dispersion measurement results after calibration. The  $D_2/2\pi$  obtained from the fitted quadric curve is 10.1 kHz, which is about 0.5 kHz larger than that from FEM results. Considering the geometric measurement and experimental measurement uncertainty, this difference is reasonable. Afterwards, the fiber

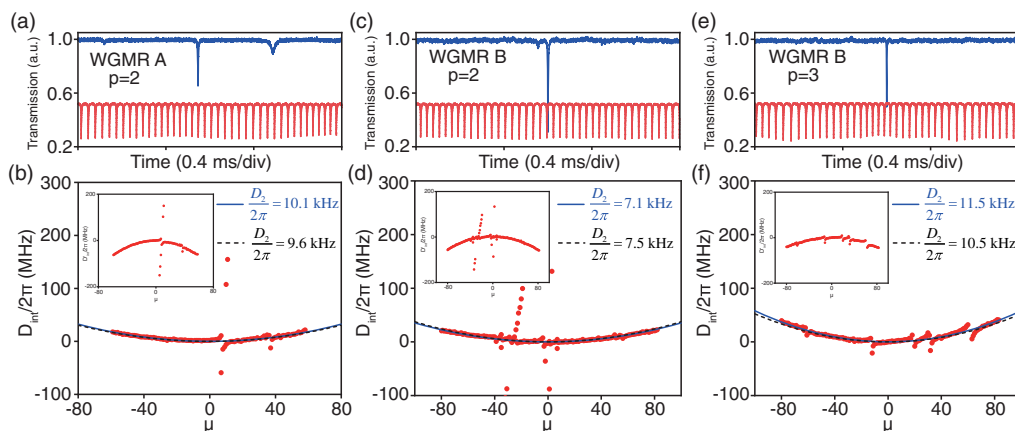


**Fig. 6.** (a) Transmission spectrum of measured mode of WGMR A with  $p = 2$ . The measured FSR of WGMR A is around 39.6 GHz. (b) Mode spectrum corresponding to (a). Red points are plotted according to Eq. (5) after calibration. Blue line is acquired by parabolic curve fitting of the red points. Black dashed line denotes the calculation results of microresonator dispersion by FEM. The values of  $D_2/2\pi$  obtained from measurement and simulation are given in the subplot, and the inset shows the results before calibration, which is the same as in Fig. 5(a). (c) Transmission spectrum of measured mode of WGMR B with  $p = 2$ . The measured FSR of WGMR B is around 29.1 GHz. (d) Mode spectrum corresponding to (c). Left part of the spectrum is perturbed by several obvious mode crossings, while the ideality of the right part is influenced by some small mode crossings. (e) Transmission spectrum of measured mode of WGMR B with  $p = 3$ . (f) Mode spectrum corresponding to (e). Five obvious avoided mode crossings appear on the spectrum, which may affect the dispersion measurement.

cavity dispersion  $D_{2F}/2\pi$  acquired from binary function fitting is directly used to measure WGM dispersion of WGMR B, and the measurement results are shown in Figs. 6(d) and 6(f) compared with the FEM results.

It is clear from Fig. 6(f) that the difference between experiments and FEM calculations is larger than those of the other two WGM families. The reason may be that the geometric error of the FEM model has a relative larger influence on higher order modes. We found that the FEM results of fundamental modes are similar in different geometric parameter settings. However, the FEM results are varied for higher order azimuthal modes, which could be thereby utilized for dispersion engineering, as shown in Section 3. Another possible reason is that this mode is affected by avoided mode crossings. Compared to the other two WGM results in Figs. 6(b) and 6(d), this mode has more obvious avoided mode crossings than other mode families, which may induce a relative larger difference in measurement results. Optical microresonators can host many transverse mode families, and these different mode families can interact with each other and distort the mode spectrum. The dispersion measurement results can be disturbed by mode crossings, and sometimes these mode interactions even change the sign of the effective dispersion in a specified wavelength range [35,59]. One way to reduce the number of mode crossings is to decrease the transverse modes that can be supported by resonators. Generally, this can be realized by limiting the cross-section area of the resonator, namely, decreasing the effective mode area, and much work has been done in this area [43,60,61]. As the  $\text{MgF}_2$  resonators measured here have a relatively larger mode area compared to that of the  $\text{SiO}_2$  wedge and  $\text{Si}_3\text{N}_4$  ring resonators, the mode crossing problem is more serious. In Fig. 7, the subplots give the measurement results of different azimuthal modes of WGMR A. Since these modes are heavily perturbed by the mode crossing phenomenon, the fitted curves show a large deviation with the measured data, making it difficult to acquire the exact dispersion of these modes. In the experiment, the fundamental mode of WGMR B was not

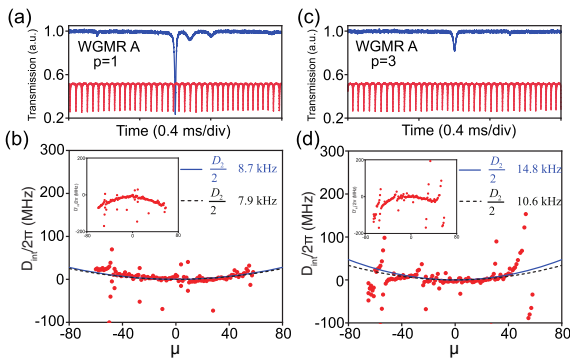


**Fig. 7.** (a) Transmission spectrum of measured mode of WGMR A with  $p = 1$ . (b) Mode spectrum corresponding to (a). The spectrum is disturbed by many small mode crossings, which makes the dispersion derived from the data inaccurate. Graphic sign definitions are the same as in Fig. 6. (c) Transmission spectrum of measured mode of WGMR A with  $p = 3$ . (d) Mode spectrum corresponding to (c). The spectrum is seriously affected by various small and large mode crossings. The parabolic curve fitting has a large deviation from the data points.

found, and the reason may lie in the unfavorable coupling position of the tapered fiber or the phase matching condition.

When measuring the FSR of a fiber cavity, it is found that the uncertainty is about  $\pm 70$  kHz, as a non-obvious difference of overlapped resonance transmission can be observed in this range. Thus, the accuracy of the fiber cavity FSR is about 0.36%, which also results in the same uncertainty of the microresonator FSR measurement. Further improvement can be carried out by better thermal stability control over both cavities during measurements.

It should be mentioned that the  $\text{MgF}_2$  resonators measured in this paper host birefringence. Since the resonators used here are  $z$ -cut, the TM mode is ordinary light and the TE mode is extraordinary light. The FEM needs to use the corresponding Sellmeier equation for the refractive index of  $\text{MgF}_2$ . Actually, the simulations of WGMRs A and B apply the Sellmeier equation of ordinary and extraordinary light, respectively. In this case, numerical simulations are more consistent with the experimental ones. This could mean that the experimentally excited modes are TM mode for WGMR A and TE mode for WGMR B.

Compared to the spectroscopy method for dispersion measurements using a stabilized commercial frequency comb reference, this approach using a fiber ring cavity etalon provides less accurate measurements. It results from the fact that this method relies on many factors. For instance, the binary function fitting means that only second order dispersion parameters of both the reference and the microresonator are taken into consideration. Moreover, the sampling rate of the oscilloscope, the dimension measurement accuracy of the resonator, and the FEM estimation accuracy of the dispersion also affect dispersion measurement. Actually, a better solution is to fully calibrate the etalon using a fiber comb reference.

Although the dimension measurement accuracy of the resonator and the FEM estimation accuracy of the dispersion can affect dispersion measurement and their influence on measurement results is difficult and complex to estimate, it is still possible to evaluate the direct measurement results of  $D_{\text{int}}$ , which is used to infer second order dispersion. The measurement of  $D_{\text{int}}$  is based on Eq. (4), and the uncertainties can be obtained by differentiation of this equation. However, uncertainties caused by two items that contain  $\delta D_1$  and  $\delta D_{1F}$  cancel each other since it is similar to the reason why we do not calibrate  $D_{1F}$  in Eq. (6). Thus, the total uncertainties of the measurement can be expressed as

$$\begin{aligned} \delta D_{\text{int}} = & D_{1F}\delta\mu_F - D_1\delta\mu + D_{2F}\mu_F\delta\mu_F \\ & + \frac{1}{2}\delta D_{2F}\mu_F^2 + \delta\Delta\omega_0 + \delta T, \end{aligned} \quad (7)$$

where  $\delta T$  is from the relative resonance frequency drift between microresonator mode and fiber cavity mode including the temperature drift. In Eq. (7),  $\delta\mu$ ,  $\delta\mu_F$  are caused by the oscilloscope sampling since the lowest point of the resonance dip may be missed by sampling. Although a Lorentz fit of the resonance dip could improve accuracy, the first two terms on the left side of the equation exhibit a maximum uncertainty of 200 kHz, which is limited by the sampling precision of the laser frequency. In an extreme case, these two terms have opposite signs, and then the total uncertainties of the first two terms are

about 400 kHz. The third and fourth terms are related to  $\mu_F$ , and this means the uncertainties become larger with  $\mu_F$  increasing. In the dispersion measurement, the maximum of  $\mu_F$  is about 60,000, and  $\delta D_{2F}$  can be estimated by considering higher dispersion in the fitting of FEM results. Hence, the largest uncertainties caused by third and fourth terms are at a level of 10 Hz and 10 kHz, respectively. Compared to the first two terms, they may be ignored.  $\delta\Delta\omega_0$  is a constant, and it makes the  $D_{\text{int}}$  curve move in one direction. Furthermore, this move can be compensated by data processing, and it should not lead to an uncertainty of dispersion measurement. As the relative thermal frequency drift is smaller than 5 MHz/min, the maximum of  $\delta T$  is estimated at a level of hundreds of kHz. From the analysis above, it is clear that the measurement precision of  $D_{\text{int}}$  is mainly limited by the sampling and thermal effect, for which an oscilloscope with a higher sampling rate and higher precision temperature control on both the microresonator and the fiber cavity can improve the precision.

## 5. CONCLUSION

In conclusion, we have demonstrated an approach based on a fiber cavity etalon for microresonator dispersion measurement. The fiber ring etalon with a high loaded  $Q$  reaching one hundred million is cost efficient and easy to prepare. The FSR of this fiber cavity is measured by sideband modulation spectroscopy, and the dispersion of the etalon is assessed by binary function fitting assisted by FEM simulated results. Using this method, dispersion profiles of two different  $\text{MgF}_2$  microresonators are obtained and analyzed, showing good agreement with numerical results. In addition to WGMRs, this method could also be applied to investigate the dispersion of other optical microresonators. Moreover, we numerically investigated the influence of geometrical parameters on WGM dispersion of  $\text{MgF}_2$  microresonators, and  $\theta_1$ ,  $\theta_2$  are preferable for dispersion engineering of high order azimuthal modes.

**Funding.** Science, Technology and Innovation Commission of Shenzhen Municipality (JCYJ20200109112805990).

**Disclosures.** The authors declare no conflicts of interest.

**Data Availability.** Data underlying the results presented in this paper are not publicly available at this time but may be obtained from the authors upon reasonable request.

## REFERENCES

- K. J. Vahala, "Optical microcavities," *Nature* **424**, 839–846 (2003).
- T. J. Kippenberg, S. M. Spillane, and K. J. Vahala, "Kerr-nonlinearity optical parametric oscillation in an ultrahigh-Q toroid microcavity," *Phys. Rev. Lett.* **93**, 083904 (2004).
- J. Li, H. Lee, T. Chen, and K. J. Vahala, "Low-pump-power, low-phase-noise, and microwave to millimeter-wave repetition rate operation in microcombs," *Phys. Rev. Lett.* **109**, 233901 (2012).
- G. Lin, A. Coillet, and Y. K. Chembo, "Nonlinear photonics with high-Q whispering-gallery-mode resonators," *Adv. Opt. Photon.* **9**, 828–890 (2017).
- L. Ge, L. Feng, and H. G. Schwefel, "Optical microcavities: new understandings and developments," *Photon. Res.* **5**, OM1–OM3 (2017).
- T. J. Kippenberg, A. L. Gaeta, M. Lipson, and M. L. Gorodetsky, "Dissipative Kerr solitons in optical microresonators," *Science* **361**, eaan8083 (2018).
- P. Del'Haye, A. Schliesser, O. Arcizet, T. Wilken, R. Holzwarth, and T. Kippenberg, "Optical frequency comb generation from a monolithic microresonator," *Nature* **450**, 1214–1217 (2008).
- M.-G. Suh, Q.-F. Yang, K. Y. Yang, X. Yi, and K. J. Vahala, "Microresonator soliton dual-comb spectroscopy," *Science* **354**, 600–603 (2016).
- Q.-F. Yang, B. Shen, H. Wang, M. Tran Anh, Z. Zhang, K. Y. Yang, L. Wu, C. Bao, J. Bowers, A. Yariv, and K. Vahala, "Vernier spectrometer using counterpropagating soliton microcombs," *Science* **363**, 965–968 (2019).
- S. B. Papp, K. Beha, P. Del'Haye, F. Quinlan, H. Lee, K. J. Vahala, and S. A. Diddams, "Microresonator frequency comb optical clock," *Optica* **1**, 10–14 (2014).
- Z. L. Newman, V. Maurice, T. Drake, J. R. Stone, T. C. Briles, D. T. Spencer, C. Fredrick, Q. Li, D. Westly, B. R. Ilic, B. Shen, M.-G. Suh, K. Y. Yang, C. Johnson, D. M. S. Johnson, L. Hollberg, K. J. Vahala, K. Srinivasan, S. A. Diddams, J. Kitching, S. B. Papp, and M. T. Hummon, "Architecture for the photonic integration of an optical atomic clock," *Optica* **6**, 680–685 (2019).
- M.-G. Suh, X. Yi, Y.-H. Lai, S. Leifer, I. Grudinin, G. Vasisht, E. Martin, M. Fitzgerald, G. Doppmann, J. Wang, D. Mawet, S. Papp, S. Diddams, C. Beichman, and K. Vahala, "Searching for exoplanets using a microresonator astrocomb," *Nat. Photonics* **13**, 25–30 (2019).
- E. Obrzud, M. Rainer, A. Harutyunyan, M. Anderson, M. Geiselmann, B. Chazelas, S. Kundermann, S. Lecomte, M. Cecconi, A. Ghedina, E. Molinari, F. Pepe, F. Wildi, F. Bouchy, T. Kippenberg, and T. Herr, "A microphotonic astrocomb," *Nat. Photonics* **13**, 31–35 (2019).
- J. Pfeifle, V. Brasch, M. Lauer, Y. Yu, D. Wegner, T. Herr, K. Hartinger, P. Schindler, J. Li, D. Hillerkuss, R. Schmogrow, C. Weimann, R. Holzwarth, W. Freude, J. Leuthold, T. Kippenberg, and C. Koos, "Coherent terabit communications with microresonator Kerr frequency combs," *Nat. Photonics* **8**, 375–380 (2014).
- A. Fülöp, M. Mazur, A. Lorences-Riesgo, P.-H. Wang, Y. Xuan, D. Leaird, M. Qi, P. Andrekson, A. Weiner, and V. Torres-Company, "High-order coherent communications using mode-locked dark-pulse Kerr combs from microresonators," *Nat. Commun.* **9**, 1598 (2018).
- D. Spencer, T. Drake, T. Briles, J. Stone, L. Sinclair, C. Fredrick, Q. Li, D. Westly, B. Ilic, A. Bluestone, N. Volet, T. Komljenovic, L. Chang, S. H. Lee, D. Y. Oh, M.-G. Suh, K. Y. Yang, M. Pfeiffer, T. Kippenberg, and S. Papp, "An integrated-photonics optical-frequency synthesizer," *Nature* **557**, 81–85 (2018).
- S.-W. Huang, J. Yang, M. Yu, B. McGuyer, D.-L. Kwong, T. Zeevinsky, and C. Wong, "A broadband chip-scale optical frequency synthesizer at  $2.7 \times 10^{-6}$  relative uncertainty," *Sci. Adv.* **2**, e1501489 (2016).
- M.-G. Suh and K. J. Vahala, "Soliton microcomb range measurement," *Science* **359**, 884–887 (2018).
- J. Riemensberger, A. Lukashchuk, M. Karpov, W. Weng, E. Lucas, J. Liu, and T. J. Kippenberg, "Massively parallel coherent laser ranging using a soliton microcomb," *Nature* **581**, 164–170 (2020).
- J. Wang, Z. Lu, W. Weiqiang, F. Zhang, J. Chen, Y. Wang, J. Zheng, S. Chu, W. Zhao, B. Little, X. Qu, and W. Zhang, "Long-distance ranging with high precision using a soliton microcomb," *Photon. Res.* **8**, 1964–1972 (2020).
- J. Feldmann, N. Youngblood, M. Karpov, H. Gehring, X. Li, M. Stappers, M. Gallo, X. Fu, A. Lukashchuk, A. Raja, J. Liu, D. Wright, A. Sebastian, T. Kippenberg, W. Pernice, and H. Bhaskaran, "Parallel convolutional processing using an integrated photonic tensor core," *Nature* **589**, 52–58 (2021).
- X. Xu, M. Tan, B. Corcoran, J. Wu, A. Boes, T. Nguyen, S. Chu, B. Little, D. Hicks, R. Morandotti, A. Mitchell, and D. Moss, "11 tops photonic convolutional accelerator for optical neural networks," *Nature* **589**, 44–51 (2021).
- J. Wang, Y. Guo, H. Liu, L. C. Kimerling, J. Michel, A. M. Agarwal, G. Li, and L. Zhang, "Robust cavity soliton formation with hybrid dispersion," *Photon. Res.* **6**, 647–651 (2018).

24. H. Weng, J. Liu, A. A. Afridi, J. Li, J. Dai, X. Ma, Y. Zhang, Q. Lu, J. F. Donegan, and W. Guo, "Directly accessing octave-spanning dissipative Kerr soliton frequency combs in an AlN microresonator," *Photon. Res.* **9**, 1351–1357 (2021).
25. J. Gu, J. Liu, Z. Bai, H. Wang, X. Cheng, G. Li, M. Zhang, X. Li, Q. Shi, M. Xiao, and X. Jiang, "Dry-etched ultrahigh-Q silica microdisk resonators on a silicon chip," *Photon. Res.* **9**, 722–725 (2021).
26. X. Zhang, H. Luo, W. Xiong, X. Chen, X. Han, G. Xiao, and H. Feng, "Numerical investigation of turnkey soliton generation in an organically coated microresonator," *Phys. Rev. A* **103**, 023515 (2021).
27. X. Wang, P. Xie, W. Wang, Y. Wang, Z. Lu, L. Wang, S. T. Chu, B. E. Little, W. Zhao, and W. Zhang, "Program-controlled single soliton microcomb source," *Photon. Res.* **9**, 66–72 (2021).
28. W. Liang, A. A. Savchenkov, V. S. Ilchenko, D. Eliyahu, D. Seidel, A. B. Matsko, and L. Maleki, "Generation of a coherent near-infrared Kerr frequency comb in a monolithic microresonator with normal GVD," *Opt. Lett.* **39**, 2920–2923 (2014).
29. X. Xue, M. Qi, and A. M. Weiner, "Normal-dispersion microresonator Kerr frequency combs," *Nanophotonics* **5**, 244–262 (2016).
30. G. Lin and Y. K. Chembo, "Phase-locking transition in Raman combs generated with whispering gallery mode resonators," *Opt. Lett.* **41**, 3718–3721 (2016).
31. G. Lin, S. Djalilo, J. M. Dudley, and Y. K. Chembo, "Universal nonlinear scattering in ultra-high Q whispering gallery-mode resonators," *Opt. Express* **24**, 14880–14894 (2016).
32. W. Jin, Q.-F. Yang, L. Chang, B. Shen, H. Wang, M. Leal, L. Wu, M. Gao, A. Feshali, M. Paniccia, K. Vahala, and J. Bowers, "Hertz-line-width semiconductor lasers using CMOS-ready ultra-high-Q microresonators," *Nat. Photonics* **15**, 346–353 (2021).
33. H.-J. Chen, Q.-X. Ji, H. Wang, Q.-F. Yang, Q.-T. Cao, Q. Gong, and X. Yi, "Chaos-assisted two-octave-spanning microcombs," *Nat. Commun.* **11**, 2336 (2020).
34. Q.-F. Yang, X. Yi, K. Y. Yang, and K. Vahala, "Spatial-mode-interaction-induced dispersive waves and their active tuning in microresonators," *Optica* **3**, 1132–1135 (2016).
35. X. Yi, Q.-F. Yang, X. Zhang, K. Y. Yang, and K. Vahala, "Single-mode dispersive waves and soliton microcomb dynamics," *Nat. Commun.* **8**, 14869 (2016).
36. C. Reimer, M. Kues, P. Roztocky, B. Wetzels, F. Grazioso, B. Little, S. Chu, T. Johnston, Y. Bromberg, L. Caspani, D. Moss, and R. Morandotti, "Generation of multiphoton entangled quantum states by means of integrated frequency combs," *Science* **351**, 1176–1180 (2016).
37. M. Kues, C. Reimer, P. Roztocky, L. Romero Cortés, S. Sciara, B. Wetzels, Y. Zhang, A. Cino, S. Chu, B. Little, D. Moss, L. Caspani, J. Azafra, and R. Morandotti, "On-chip generation of high-dimensional entangled quantum states and their coherent control," *Nature* **546**, 622–626 (2017).
38. J. Riemensberger, K. Hartinger, T. Herr, V. Brasch, R. Holzwarth, and T. J. Kippenberg, "Dispersion engineering of thick high-Q silicon nitride ring-resonators via atomic layer deposition," *Opt. Express* **20**, 27661–27669 (2012).
39. W. C. Jiang, J. Zhang, N. G. Usechak, and Q. Lin, "Dispersion engineering of high-Q silicon microresonators via thermal oxidation," *Appl. Phys. Lett.* **105**, 031112 (2014).
40. A. Eshaghian, D. Timucin, K. Thyagarajan, T. Wunderer, N. Johnson, and D. Schwartz, "Advanced dispersion engineering of a III-nitride micro-resonator for a blue frequency comb," *Opt. Express* **28**, 30542–30554 (2020).
41. Y. Okawachi, K. Saha, J. Levy, Y. Wen, M. Lipson, and A. Gaeta, "Octave-spanning frequency comb generation in a silicon nitride chip," *Opt. Lett.* **36**, 3398–3400 (2011).
42. S. Kim, K. Han, C. Wang, J. Jaramillo-Villegas, X. Xue, C. Bao, Y. Xuan, D. Leaird, A. Weiner, and M. Qi, "Dispersion engineering and frequency comb generation in thin silicon nitride concentric microresonators," *Nat. Commun.* **8**, 372 (2017).
43. K. Y. Yang, K. Beha, D. Cole, X. Yi, P. Del'Haye, H. Lee, J. Li, D. Y. Oh, S. Diddams, S. Papp, and K. Vahala, "Broadband dispersion-engineered microresonator on a chip," *Nat. Photonics* **10**, 316–320 (2016).
44. I. Grudinin and N. Yu, "Dispersion engineering of crystalline resonators via microstructuring," *Optica* **2**, 221–224 (2015).
45. S. Fujii, Y. Hayama, K. Imamura, H. Kumazaki, Y. Kakinuma, and T. Tanabe, "All-precision-machining fabrication of ultrahigh-Q crystalline optical microresonators," *Optica* **7**, 694–701 (2020).
46. S. Fujii and T. Tanabe, "Dispersion engineering and measurement of whispering gallery mode microresonator for Kerr frequency comb generation," *Nanophotonics* **9**, 1087–1104 (2020).
47. P. Del'Haye, O. Arcizet, M. Gorodetsky, R. Holzwarth, and T. Kippenberg, "Frequency comb assisted diode laser spectroscopy for measurement of microcavity dispersion," *Nat. Photonics* **3**, 529–533 (2009).
48. M. J. Thorpe, R. J. Jones, K. D. Moll, J. Ye, and R. Lalezari, "Precise measurements of optical cavity dispersion and mirror coating properties via femtosecond combs," *Opt. Express* **13**, 882–888 (2005).
49. S. Fujii, S. Tanaka, M. Fuchida, H. Amano, Y. Hayama, R. Suzuki, Y. Kakinuma, and T. Tanabe, "Octave-wide phase-matched four-wave mixing in dispersion-engineered crystalline microresonators," *Opt. Lett.* **44**, 3146–3149 (2019).
50. G. Lin, J. Fürst, D. V. Strekalov, I. S. Grudinin, and N. Yu, "High-Q UV whispering gallery mode resonators made of angle-cut BBO crystals," *Opt. Express* **20**, 21372–21378 (2012).
51. J. Li, H. Lee, K. Y. Yang, and K. Vahala, "Sideband spectroscopy and dispersion measurement in microcavities," *Opt. Express* **20**, 26337–26344 (2012).
52. X. Yi, Q.-F. Yang, K. Y. Yang, M.-G. Suh, and K. Vahala, "Soliton frequency comb at microwave rates in a high-Q silica microresonator," *Optica* **2**, 1078–1085 (2015).
53. H. Lee, T. Chen, J. Li, K. Y. Yang, S. Jeon, O. Painter, and K. J. Vahala, "Chemically etched ultrahigh-Q wedge-resonator on a silicon chip," *Nat. Photonics* **6**, 369–373 (2012).
54. H. Zhou, Y. Geng, W. Cui, S.-W. Huang, Q. Zhou, K. Qiu, and C. Wong, "Soliton bursts and deterministic dissipative Kerr soliton generation in auxiliary-assisted microcavities," *Light Sci. Appl.* **8**, 50 (2019).
55. T. Herr, V. Brasch, J. Jost, C. Wang, N. Kondratiev, M. Gorodetsky, and T. Kippenberg, "Temporal solitons in optical microresonators," *Nat. Photonics* **8**, 145–152 (2012).
56. L. He, Y. Xiao, C. Dong, J. Zhu, V. Gaddam, and L. Yang, "Compensation of thermal refraction effect in high-Q toroidal microresonator by polydimethylsiloxane coating," *Appl. Phys. Lett.* **93**, 201102 (2008).
57. M. J. Weber, *Handbook of Optical Materials* (CRC Press, 2003).
58. G. Lin and Y. Chembo, "On the dispersion management of fluorite whispering-gallery mode resonators for Kerr optical frequency comb generation in the telecom and mid-infrared range," *Opt. Express* **23**, 1594–1604 (2015).
59. T. Herr, V. Brasch, J. D. Jost, I. Mirgorodskiy, G. Lihachev, M. L. Gorodetsky, and T. J. Kippenberg, "Mode spectrum and temporal soliton formation in optical microresonators," *Phys. Rev. Lett.* **113**, 123901 (2014).
60. A. Kordts, M. H. Pfeiffer, H. Guo, V. Brasch, and T. J. Kippenberg, "Higher order mode suppression in high-Q anomalous dispersion silicon microresonators for temporal dissipative Kerr soliton formation," *Opt. Lett.* **41**, 452–455 (2016).
61. I. S. Grudinin, V. Huet, N. Yu, A. B. Matsko, M. L. Gorodetsky, and L. Maleki, "High-contrast Kerr frequency combs," *Optica* **4**, 434–437 (2017).